metals

MDPI

Article

Numerical Modelling of Microstructure Evolution in Friction Stir Welding (FSW)

Narges Dialami *, Miguel Cervera and Michele Chiumenti

International Center for Numerical Methods in Engineering (CIMNE), Technical University of Catalonia, Campus Norte UPC, 08034 Barcelona, Spain; miguel.cervera@upc.edu (M.C.); michele@cimne.upc.edu (M.C.)
* Correspondence: narges@cimne.upc.edu; Tel.: +34-93-401-6529

Received: 6 February 2018; Accepted: 9 March 2018; Published: 14 March 2018

Abstract: This work studies the metallurgical and microstructural aspects of Friction Stir Welding (FSW) in terms of grain size and microhardness. The modelling is based on the combination of an apropos kinematic framework for the local simulation of FSW processes and a material particle tracing technique for tracking the material flow during the weld. The resulting grain size and microhardness values are validated with experimental observations from an identical processed sample. A Sheppard-Wright constitutive relation is adopted to describe the mechanical behavior of AZ31 Mg alloy considered in this work. The strain rate and temperature histories obtained from the numerical model are stored on the tracers. The relationship among the grain size, microhardness, strain rate, and temperature is obtained using Zener-Hollomon parameter and Hall-Petch relationship. A linear description relates the logarithm of average grain size to the logarithm of Zener-Hollomon parameter. The relationship between microhardness and average grain size stands away from the linear trend.

Keywords: FSW; material tracing; grain size; microhardness

1. Introduction

In the FSW process, a fast-rotating tool moves along the joining line, mixing the deformed material and altering the microstructure of the unprocessed parts. The impact of the tool rotation rate is on the material flow through wavering the frictional heat input and volume of material conveyed and released, having a great effect on the creation and shape of the stir zone [1].

Friction Stir Welding (FSW), being a solid state joining technology, refines the grain size due to recrystallization arising from both frictional heating and plastic dissipation during the welding. The fine-grained microstructures results in exquisite mechanical properties in the weld. Grain refinement in metallic materials drastically increases yield strength while improving the toughness.

Based on the microstructural characterization of grains and precipitates, various zones are identified in the FSW joint (Figure 1): Base Metal (BM), Nugget Zone (NZ), Thermo-Mechanically Affected Zone (TMAZ), and Heat Affected Zone (HAZ). NZ is where the grain size is significantly refined due to the dynamic recrystallization caused by intense plastic deformation and frictional heating during FSW. The TMAZ, lying between NZ and HAZ, is the zone where the material is plastically deformed and heated, but, insufficient to cause recrystallization. The HAZ encounters just a heating effect, with no mechanical deformation. The grain structures are like that of the base material, yet some recently shaped grains surrounding the large grains originated from static recrystallization exist. The post weld mechanical properties are altogether influenced by the microstructural changes of the mentioned zones. Figure 1 shows the macrostructure of the FSW joint, where AS and RS denote the advancing and retreating sides, respectively.

Figure 1. Macrostructure of a FSW joint [2].

Grain evolution in these welding zones is one of the key elements for controlling the welding quality and for understanding the FSW mechanism.

Several studies have been devoted to investigating material flow visualization and corresponding microstructural alteration during FSW.

In the work of Pashazadeh et al. [3], a numerical model is developed for the prediction of temperature profile, effective plastic strain, and material flow in FSW of copper plates. The material flow pattern utilizing point tracking is in great concurrence with the examinations.

In the work of Padmanaban et al. [4], the temperature profile and material flow during FSW of dissimilar alloys (AA2024 and AA7075) using a cylindrical tool are predicted by a steady-state, visco-plastic Computational Fluid Dynamics (CFD) model. They demonstrated that increasing the tool rotation speed and the shoulder diameter increases the material flow, while increasing the welding speed decreases the material flow in the stir zone.

In Dialami et al. [5,6], the material flow in FSW process is modelled using a material tracing method. The tracer trajectories are computed using the Backward Euler with Sub-stepping (BES), the 4-th order Runge-Kutta (RK4) and the Back and Forth Error Compensation and Correction (BFECC). The material flow pattern is compared with the experimental evidence.

In the work of Masaki et al. [7], the recrystallized grains of the stir zone of 1050 Al after FSW process is simulated. They take into account both the creation of recrystallized grains during the deformation procedure and the grain growth during the following cooling phase. It is performed via a sequence of the plane-strain compression test at different strain rates and the resulting cooling following the cooling cycle of FSW.

Zhang et al. [8] used an adaptive re-meshing finite element model to predict the temperature and material behavior during FSW of AA6082-T6. The Monte Carlo (MC) strategy with nucleation in each MC step is utilized for the analysis of the grain development in FSW. They investigated that an increase in the tool rotational speed or the tool shoulder diameter increases the overall grain size and the width of the welding zones.

In the work of Chang et al. [9], the relationship between the grain size, strain rate and temperature in FSW processing on AZ31 Mg alloy is analyzed. The grain orientation distribution is additionally considered utilizing the X-ray diffraction.

In the work of Pan et al. [10], a smoothed particle hydrodynamics (SPH) model for FSW is adopted. The temperature history and distribution, grain size, microhardness and additionally the texture evolution are displayed.

In the work of Darras et al. [11], friction stir processing is used to refine the microstructure and features of AZ31B-H24 magnesium alloy. The impact of a few process parameters on thermal histories, final microstructure and properties are examined.

An experimentally established finite element model is considered in the work of Ammouri et al. [12] to appraise the strain rate and the temperature values for calculating the Zener-Hollomon parameter of twin-roll-cast (TRC) AZ31B after friction stir processing.

Fratini et al. [13] link an artificial neural network to a finite element model to predict the average grain size values in the FSW process starting from experimental data and numerical results as input.

Saluja et al. [14] present a cellular automata-coupled finite element (CAFE) model to estimate the grain size profile during FSW. The simulation is performed applying thermal and strain rate analytical models on the FSW elements using ABAQUS6.8.

Although a vast number of studies on microstructure of the material are available, a robust numerical model able to predict the microstructure evolution in the material after FSW process is still lacking. The relationship between the trajectory, the temperature and strain rate evolution and the final position of the flowing material tracers and the grain growth has not been investigated in depth. Also, recrystallization during FSW takes place in the presence of rapid transients and severe gradients in strain rate and temperature, which further complicates the microstructural characterization.

In this work, we strive to upgrade the FSW model formerly established by the authors [15–20] with a microstructural model able to predict the average grain size and microhardness. This model is not only fast and accurate and enriched with the enhanced friction model but also incorporates a material tracing technique to track the position of each material tracer during the weld from the initial position until the final location. The material tracing technique allows the prediction of the final grain size by incorporating the thermo-mechanical histories extracted from the finite element model.

In the present work, the microstructural characterization for the AZ31 Mg alloy is that proposed in reference [9] during friction stir processing (it has been also used in e.g., [7,10,12,21]). FSW processed magnesium alloys are found to have noticeable grain refinement [22]. Moreover, joining magnesium alloys using solid-state processes such as FSW has many advantages over conventional welding technologies [23,24]. Among others, it avoids defects such as hot cracking and partial melting zone.

The numerical simulation performed here is compared against the experimental data presented in the work of Darras et al. [11]. The proposed model defines a significant forward step towards accounting for microstructural effects within the overall thermomechanical FSW model that has proven to be a robust approach to now.

The outline of the paper is as follows. Section 2 presents briefly the solution strategy incorporated in this work to obtain the thermomechanical results and to find the material tracer position. Then, the microstructural evolution in terms of grain growth and microhardness for AZ31 Mg alloy is introduced. At the end, a 3D numerical example is presented with the aim to compare the calculated grain size and microhardness with the experimental data of reference [11].

2. Solution Strategy

The two-stage strategy for the simulation of FSW processes lately developed by the authors [18] is used in this work. The strategy includes two thermo-mechanical simulation phases: the speed-up stage and the periodic stage.

The speed-up stage aims at reaching the steady-state close to the final periodic state. This is accomplished by accelerating the inertial term in the energy balance equation using a speed-up factor to decrease the thermal capacity. In this stage, the pin tool is kept in a fixed configuration within the considered Eulerian framework. Thus, no periodic solution due to the pin rotation is obtained.

The periodic stage starts from the thermo-mechanical results (temperature and velocity fields) acquired from the first stage as initial conditions. The FSW analysis using non-cylindrical pin-shapes leads to a periodic solution according to the real rotation of the pin. Further details on the strategy can be consulted in reference [18].

In both stages, the mechanical problem is quasi-static due to the low values of Reynolds number in the FSW process. Contrariwise, a transient thermal problem is solved in both stages to accurately evaluate the flow characteristics during the rotation of the asymmetrical tool.

Figure 2 illustrates the summarized features of both simulation phases.

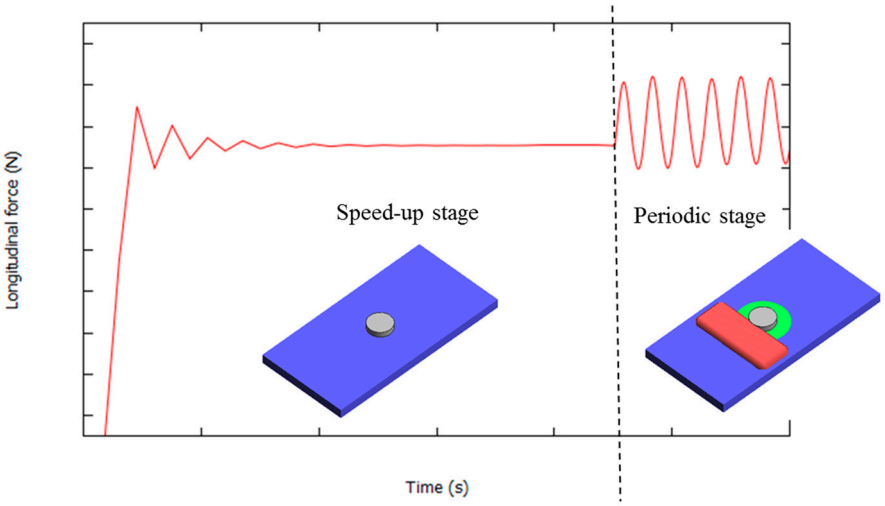

	Speed-up stage	Periodic stage
Problem	Coupled thermo-mechanical	Coupled thermo-mechanical
Computational framework	Eulerian (blue)	ALE (green)+Eulerian (blue)
Material particles (red)	Not included	Included

Figure 2. Two-stage strategy concept.

2.1. Kinematic Framework

This work focuses on the periodic stage of the simulation where the material flow due to the rotating and advancing movement of the tool are accounted for. It is also feasible to determine the thermo-mechanical history that the material experiences. In this stage, an apropos kinematic framework is adopted using the Arbitrary Lagrangian Eulerian (ALE), Eulerian and Lagrangian schemes.

The use of an apropos kinematic framework in a FSW problem conveniently allows dealing with arbitrary pin profiles and applying the boundary conditions. A domain including the tool and the Thermo-Mechanically Affected Zone (TMAZ) is considered. The Lagrangian formulation is used for the rigidly rotating tool. ALE and Eulerian formulations are used for the TMAZ and the remaining part of the analyzed domain, respectively (see Figure 2). Details on the apropos kinematic framework are given in reference [15].

2.2. Material Tracing

In the ALE and Eulerian frameworks, the mesh representing the workpiece does not follow the material movement. Therefore, to find the final locations of the flowing material points and their microstructure evolution, a material tracing technique needs to be executed.

The grain sizes in the last locations of the followed material points can be then processed from the temperature and strain rate histories extracted from the finite element model.

The heat generated during the FSW process augments the temperature at the workpiece starting at the contact surface with the tool and reduces the material flow stress. Consequently, plastic flow of the material increases resulting in generation of very large plastic deformation and friction at tool-workpiece contact interface. Thus, the temperature rises, and its distribution causes the microstructure evolution in the welding zone. The modified grain size and grain boundary character affect the mechanical properties of the weld. Therefore, to predict correctly the microstructure evolution, it becomes necessary to obtain information regarding temperature distribution and flow behavior during FSW as the variation in the grain sizes of the welding zone are characterized by the deformation and the temperature histories in the FSW procedure. In the light of the material flow rule of each followed tracer, the histories of the strain rates and the temperatures can be ascertained and additionally utilized for prediction of the grain size evolutions in the welding area. Moreover, knowing the material

tracer motion assists to determine the location of various welding zones on the cross section of the friction stir weld.

To perform material tracing, a set of tracers is initially distributed in the domain representing the material.

Figure 3 shows the domain used to perform a FSW simulation with material tracing. Note that material tracers are not grains themselves.

Then the tracing technique permits following the motion of each material tracer and find its position at each time step of the simulation during the weld.

The position of a tracer at time, $\mathbf{X}(t)$, is obtained by solving the following equation at each time-step of the simulation:

$$\mathbf{X}(t) = \mathbf{X}_0 + \int_0^t \mathbf{V}(\mathbf{X}(t), t)\mathrm{d}t \tag{1}$$

where $\mathbf{X}_0$ is the initial position of each tracer and $\mathbf{V}(\mathbf{X}(t), t)$ is the velocity at its present position (Figure 4).

Having computed the velocity of the material tracers, their position is found by performing the appropriate time integration. The 4-th order Runge-Kutta (RK4) time integration scheme is the one used in this work. This method is chosen due to its capability of the exact integration of a circular trajectory (typical profile path in FSW).

A search algorithm is executed to find the finite element where each tracer is located at each time step. The velocity and temperature of the material tracers are interpolated from the nodal velocities and temperature of the finite element, respectively. The strain rate ($\dot{\varepsilon}$) can be also computed from the velocity field in the finite element through its symmetric gradient ($\dot{\varepsilon} = \nabla^s \mathbf{v}$).

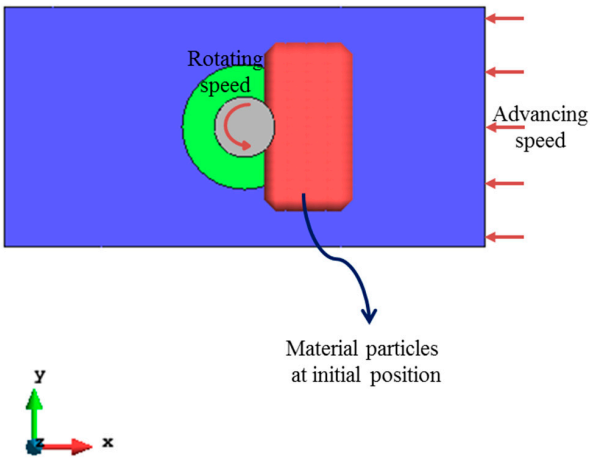

Figure 3. Domain decomposition to perform a FSW simulation using material tracing technique.

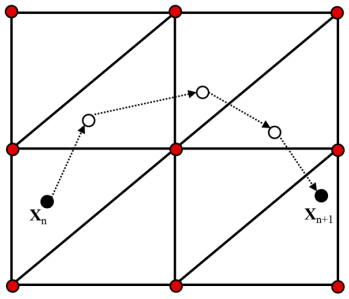

Figure 4. Position of a material tracer during 4 sub-time steps.

Further details on the implemented material tracing technique are given in references [5,6].

2.3. Heat Generation

Plastic dissipation and friction are the origins of heat generation calculated at the mechanical partition of the problem and coupled to the thermal partition.

The viscoplastic dissipation (D_{mech}) reads:

$$D_{mech} = \beta \mathbf{s} : \dot{\varepsilon}, \tag{2}$$

where β is the fraction of plastic dissipation converted into heat and $\mathbf{s}$ is the stress deviator.

Friction phenomena are modelled by an enhanced friction model proposed by the authors in [19]. This model considers the impact of non-uniform pressure distribution regularly seen under the FSW tool which brings about higher friction before the tool and lower friction at the back. This non-uniformity leads to the generation of the significant transversal force recorded in the experimental measurements which cannot be modeled using common friction laws such as Coulomb or Norton [19]. The enhanced friction law reads:

$$\boldsymbol{\tau}_T = a(x,T)\|\Delta \mathbf{v}_T\|^q \mathbf{n}, \tag{3}$$

where $\boldsymbol{\tau}_T$ is the friction shear stress, q is the sensitivity parameter ($0 \leq q \leq 1$) and $\Delta \mathbf{v}_T$ is the respective slip velocity among the contact surfaces of the tool and the workpiece. $\mathbf{n} = \frac{\Delta \mathbf{v}_T}{\|\Delta \mathbf{v}_T\|}$ is the slip direction. The consistency parameter $a(x,T)$ at the tool/workpiece interface is non-uniformly expressed as:

$$a(x) = 0.5\left(a_{\max} + a_{\min} + (a_{\max} - a_{\min}) \tanh \frac{x}{R/6}\right), \tag{4}$$

being x the position relative to the rotation axis at the tool/workpiece interface and projected along the welding direction and R the shoulder radius. Friction tractions exhibit variations between maximum to minimum value from the heading side of the shoulder to the backside. Since the temperature of the working zone does not change considerably, it is assumed that the maximum ($a_{\max}$) and minimum ($a_{\min}$) consistency parameters depend on the average working temperature only.

2.4. Flow Stress

To model the flow stress of the magnesium workpiece a Sheppard-Wright constitutive relation is adopted (Sheppard et al. [25]). According to this model, the effective viscosity μ_{eff} is characterized as a function of effective flow stress σ_e (i.e., norm of deviatoric stress) and effective strain rate $\dot{\bar{\varepsilon}}$ (i.e., norm of deviatoric strain rate) as

$$\mu_{eff} = \frac{\sigma_e}{3\dot{\bar{\varepsilon}}}, \tag{5}$$

where the effective stress is a function of the strain rate and the temperature field (below the metal's solidus temperature) and is expressed as

$$\sigma_e = \frac{1}{\alpha} \sinh^{-1}\left(\left(\frac{Z}{A}\right)^{\frac{1}{n}}\right), \tag{6}$$

where the material constants α, A and n are computed by fitting the experimental response of the material. Note that all these parameters are independent of temperature. The temperature compensated strain rate parameter or Zener-Hollomon parameter (Z) associates the temperature and the strain rate in the form

$$Z = \dot{\bar{\varepsilon}} \exp\left(\frac{Q}{RT}\right), \tag{7}$$

where $\dot{\bar{\varepsilon}} = \sqrt{\frac{2}{3}}(\dot{\varepsilon} : \dot{\varepsilon})^{1/2}$ is the equivalent strain rate, Q is the activation energy, R = 8.314 J/mol·K is the gas constant and T is the absolute temperature.

The activation energy Q for AZ31 Mg alloy is about 129 kJ/mol (Tello et al. [26]).

3. Microstructure Evolution, Grain Size and Microhardness

The modeling of the metallurgical and microstructural aspects of FSW is described in this section. Material mixing and heat generation in FSW procedures lead to considerable microstructure and material properties alterations. The continuous dynamic recrystallization phenomena contribute to grain refinement in the weld and strongly influence the final joint strength.

To predict the average grain size and microhardness, the Zener-Hollomon parameter and the Hall-Petch relationship are used.

The temperature and strain rate values are computed from the finite element analysis model at each time step of the second (periodic) stage and are used in the calculation of Zener-Hollomon parameter for each tracer of the moving material placed in the finite element model. The methodology used in this work considers the effect of the steep gradients of strain rates and temperature that occur in the stir zone. In fact, they are fully considered in the local analysis of the FSW process and they are significant. To this end, an apropos kinematic framework is used, with the stir zone appropriately modeled using an ALE/Eulerian formulation. To obtain the strain rate and temperature history of the material tracers, these tracers are followed during the weld as they pass through the critical zone where the most significant changes of strain rate and temperature occur. These variations are recorded in the tracer history and the computation of the Zener-Hollomon parameter.

The Zener-Hollomon parameter is identified with the subsequent grain size because of dynamic recrystallization in extruded magnesium-based alloys (Wang et al. [21]). In the reference [9], dynamic recrystallization is given as the cause of the fine grains in friction stir processed Al and Mg alloys samples. The relationship between the Zener-Hollomon parameter and the recrystallized grain size for AZ31 Mg alloy is proposed by Chang et al. [9]. A linear relationship between the average grain size values vs. Zener-Hollomon parameter trends in logarithmic scale according to Chang et al. [9] yields

$$\ln(d) = 9.0 - 0.27 \ln(Z), \tag{8}$$

where d is the average grain size in μm. The coefficients are slightly different from those obtained earlier by Wang et al. [21] and Huang et al. [27]. They confirmed from the experimental data on the grain size and Zener–Hollomon parameter that the resulting grain sizes basically follow similar trends irrespective of the deformation path.

This relationship is used also in the other works [10]. A similar log-linear relationship is also presented in references [12,21]. For 6063 Al alloys, Sato et al. [7] define a similar relationship between grain size and temperature.

Figure 5 shows the logarithmic relationship between grain size and the Zener-Hollomon parameter, Equation (8), used in this work.

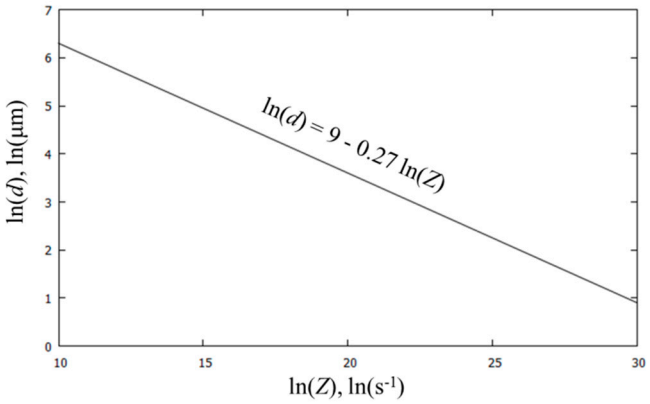

Figure 5. Logarithmic relationship between grain size and the Zener-Hollomon parameter.

Through this relationship, the grain size is correlated with the local temperature compensated strain rate and, in turn, with the local material velocities. The average grain size increments by expanding the working temperature and diminishing the strain rate.

The above-mentioned equation is valid for a working zone characterized by equivalent strain rate and temperature higher than 0.5 s^{-1} and 227 °C, respectively. The temperature range of magnesium alloys recrystallization is 250–480 °C (Fatemi-Varzaneh et al. [28]).

Microhardness is inhomogeneously dispersed in FSW welds. This distribution is identified with the grain size, crystallographic texture, dislocation density, and distribution of hardening phases. According to the Hall-Petch relationship, the Vickers microhardness, H_v, in the processing zone is obtained (Chang et al. [9]) as

$$H_v = 40 + 72d^{-0.5}, \quad (9)$$

Therefore, reducing the grain size increases the microhardness in FSW welds.

Figure 6 shows the non-linear relationship between grain size and the microhardness.

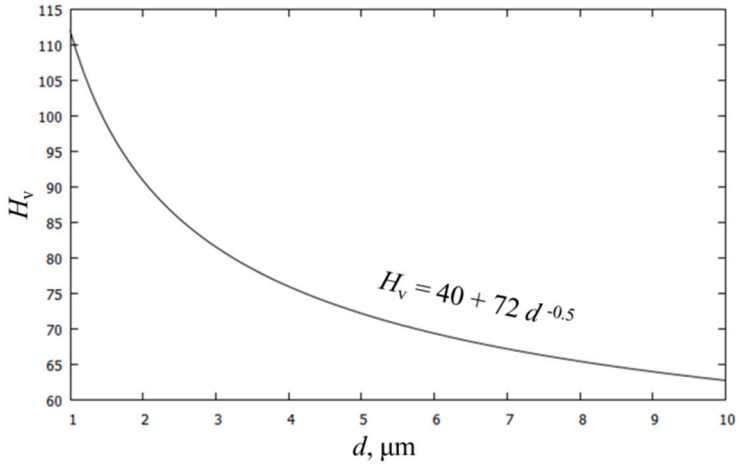

Figure 6. Hall-Petch relationship for grain size and microhardness.

Finally, it should be noted that recrystallization during FSW takes place in the presence of rapid transients and severe gradients in strain rate and temperature. The numerical model for FSW here contemplated can record the full history of the strain rate and the temperature for each tracer, as it travels across the working zone. However, the microstructural characterization described in this Section, from reference [9], takes into account the peak values of the state thermo-mechanical variables, but not their rates of change. Introducing such a refinement in the microstructural model is fully feasible in the present numerical strategy, provided that the physical model and its experimental validation are available.

4. Model Validation

The aim of this section is to validate the numerical model proposed here for the prediction of the microstructural behavior by comparing the computed results with experimental data provided in the literature. It compares the numerical results in terms of temperature, average grain size and microhardness with the experimental data of reference [11]. The geometrical data and the selected material are chosen according to the experimental set-up presented in the work of Darras et al. [11].

The cylindrical tool consists of a pin with 6.35 mm diameter, 3.048 mm height, and a 12.7 mm diameter shoulder. A workpiece domain of 100 × 50 × 3.175 mm^3 is considered. Rotational and advancing velocities are 1200 rpm and 0.0093 m/s, respectively. Boundary conditions are defined by prescribing the advancing velocity of the workpiece, opposite to the weld direction (relative movement) and rotating speed is applied to the tool.

The workpiece material is AZ31 Mg alloy. Its mechanical properties corresponding to the Sheppard-Wright constitutive model are α = 1.9 (Mpa)$^{-1}$, A = 7.78 × 10^{8} s^{-1}, n = 4.36 and Q = 129 × 10^{3} J/mol (Tello et al. [26]). Its thermal properties are density = 1777 kg/m^{3}, thermal conductivity = 400 W/m K and specific heat = 1164 J/kg K (Hu et al. [29]).

It is considered that 90% of the plastic dissipation is transferred into heat. The analysis adopts the minimum and maximum friction coefficients equal to $a_{\min}$ = 2.35 × 10^{7} and $a_{\max}$ = 4.7 × 10^{8} at tool/workpiece interfaces, respectively.

The workpiece is discretized by 360,000 tetrahedral elements and 70,000 nodes, approximately. 200,000 material tracers are distributed in the domain of 30 × 13.5 × 3.175 mm^{3} covering the entire thickness of the workpiece and the working zone.

This work considers a set of tracers representing the material in a part of the domain. These material tracers move following the material flow. At each time step their position is found and the temperature and strain rate are recorded on the tracer. From these data the grain size is calculated for each tracer. Recall that material tracers are not grains themselves.

Figure 7 shows the mesh detail used for different parts of the domain and a magnified mesh view on the pin and stir zone.

At the first stage, the temperature distribution obtained from the thermo-mechanical numerical model at the steady state using an Eulerian formulation is compared with the temperature variation recorded in the experiment performed by Darras et al. [11] for the above mentioned rotational and advancing velocities.

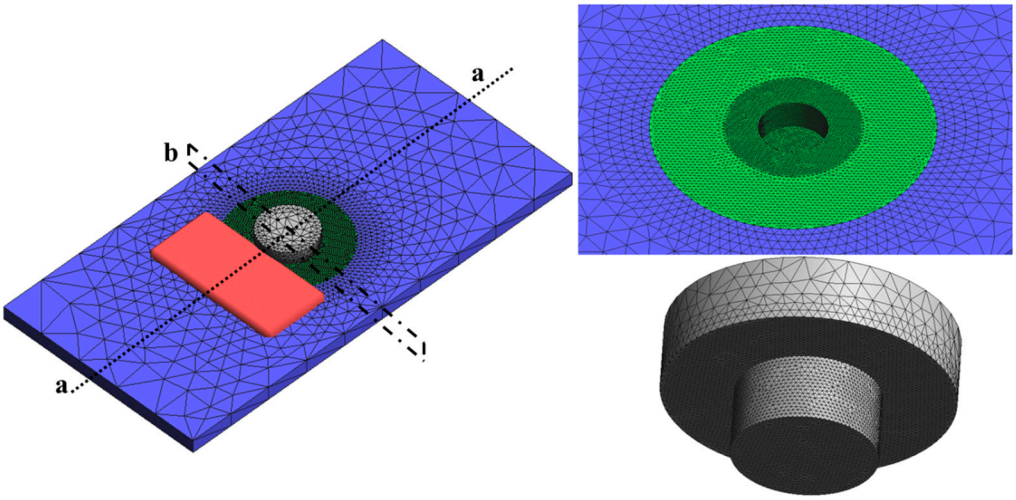

Figure 7. Mesh detail used for different parts of the domain.

Figure 8 demonstrates the temperature acquired from the numerical analysis drawn along the line aa (illustrated in Figure 7) on the top surface compared to the experimental measurements under identical processing conditions.

Computational and experimental temperature trends are in good agreement, presenting higher temperature values in front of the tool than in the backside. The temperature increases close to the tool and decreases with the distance from the tool. The maximum temperature is below the melting point of the AZ31 Mg alloy (618 °C).

Figures 9 and 10 show the distribution of temperature T and logarithmic equivalent strain rate $\dot{\bar{\varepsilon}}$ in a vertical cross section of the workpiece (plane b in Figure 7) in an Eulerian (spatial) framework.

Regarding the metallurgical aspects, Figure 11 shows the final position of the material tracers after passing through the FSW tool. To reach this configuration, 60 cycles of the second (periodic) stage of the thermo-mechanical analysis are performed from the initial configuration of Figure 7.

The maximum temperature T and equivalent strain rate $\dot{\bar{\varepsilon}}$ are recorded for each material tracer. They are in turn used for the calculation of the average grain size and microhardness.

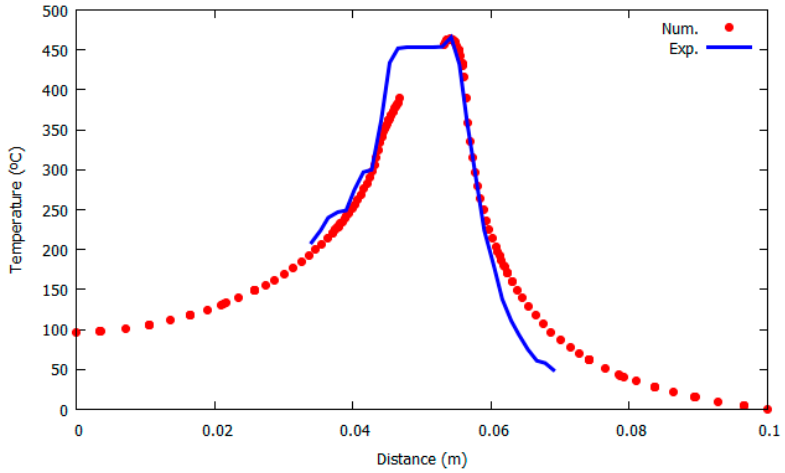

Figure 8. Comparison between the computational and experimental temperatures along the line aa.

Figure 9. Temperature of the workpiece on the transversal section in the Eulerian (spatial) framework.

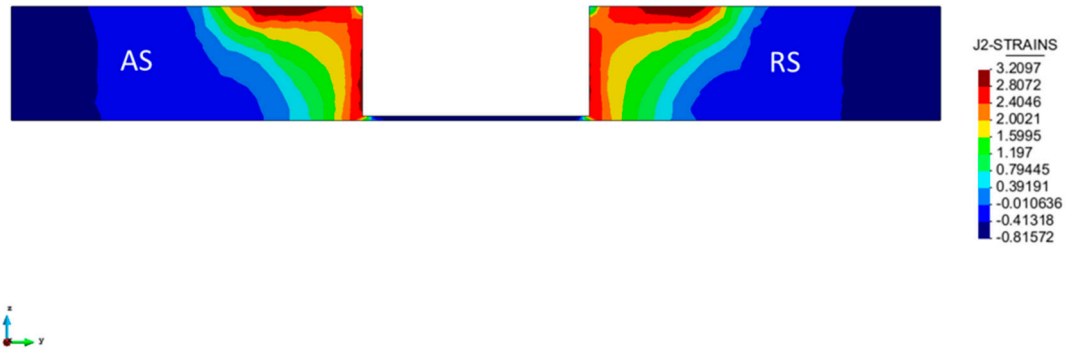

Figure 10. Logarithmic equivalent strain rate on the workpiece transversal section in the Eulerian (spatial) framework.

Figures 12 and 13 illustrate the distribution of the mentioned parameters in a vertical cross section of the material tracer set (plane c in Figure 11). The stain rate at the advancing side is greater than at the retreating side because of the distinctive material flow designs. The maximum temperature and logarithm of equivalent strain rate recorded at the tracers are 490 °C and 3.2 s^{-1}, respectively. The reported limits of dynamic recrystallization identified by Darras et al. [11] are temperature and strain rate values exceeding 227 °C and 0.5 s^{-1}.

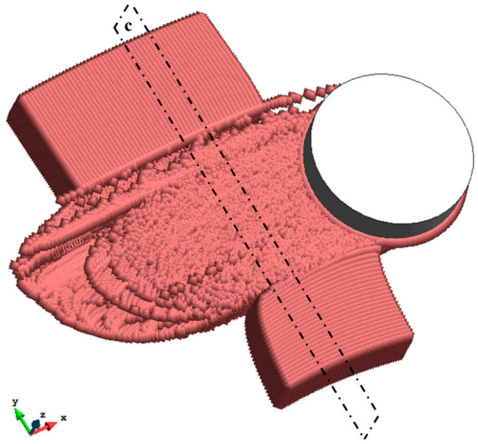

Figure 11. Final position of the material tracers after passing through the tool.

The computed values of the Zener-Hollomon parameter in the transversal section on the tracers (plane c in Figure 11) in logarithmic scale are presented in Figure 14. The calculated logarithmic values of Zener-Hollomon parameter, just if the recrystallization limits are surpassed, vary in the range of 10–13. It can be seen from the same figure the coupled effect of increasing strain rate and temperature on the Zener-Hollomon parameter. The Zener-Hollomon parameter increases by the temperature diminution or by the strain rate rise. It is found that both the temperature and strain rate affect the growth of the Zener-Hollomon parameter. However, the component that has a major impact on this trend is the temperature, resulting in the total decreasing of Zener-Hollomon parameter.

Figure 15a presents the working and non-working zones according to the limits defined by Darras et al. [11]. The working zone is where temperature and equivalent strain rate values exceed 227 °C and 0.5 s^{-1}, respectively. The calculated grain size in μm is shown in the Figure 15b on the material tracers (plane c in Figure 11).

The processed material is portrayed by non-uniform grain sizes differing from 1 to 10 μm with an average grain size of 4.9 μm. The average grain size obtained from the numerical model is in accordance with the experimental value of 4.2 μm presented in Darras et al. [11]. It is found that the resultant grain size is a combination of grain refinement, because of the expanding strain rate, and grain growth, because of the temperature rise. This behavior is confirmed also by Rodriguez et al. [30]. At constant temperature, the grain size decreases for increasing strain rate. Conversely, at constant strain rate, the grain size increments as the temperature increases. Therefore, the greatest grain refinement occurs at lower temperature and higher strain rates.

Figure 16 (reproduced from ref. [11]) presents the histogram of grain intercept obtained from a micrograph of size 70 × 80 μm^2, a small fraction of the overall domain (approx. 100 × 50 mm^2 in size). Figure 17 shows the grain size distribution after FSW on the set of material tracers located within the working zone. It presents the grain size (X axis) versus the number of material tracers (Y axis). It shows how many of the material tracers used in the numerical modeling fall into a certain range of grain size. These two histograms of grain size are not directly comparable. The reasons for this are:

(1) The numerical distribution of grain size is obtained for the whole working zone, while the experimental micrograph is just one sample.
(2) Tracers are not grains, they are material sampling points used for evaluating the gran size (they have not information of grain shape).

However, the average grain size of the micrograph analysis (4.2 μm) is statistically representative of the experimental result. This compares remarkably well with the numerical prediction of 4.9 μm.

As reported in the work of Darras et al. [11], the grain structure after the welding process is more equiaxed and homogenized. The FSW process leads to microstructure refinement of the workpiece

from the original state to an average value of 4.9 μm. The distribution of the grain size is focused on the left-hand side providing greater refinement and a homogenous equiaxed microstructure. The finer and more homogenous microstructure of the workpiece after the FSW process boosts the superplastic behavior of the material [31].

Figure 18 presents the calculated hardness on a vertical section of the tracer set through the thickness of the working zone. The distribution of the hardness varies between 60 and 80. The average calculated hardness is 73 while in the work of Darras et al. [11] the experimental hardness is around 70. As the temperature increases more softening of the material due to grain growth occurs. As indicated by the Hall-Petch relationship, the hardness is contrarily proportional to the grain growth. Therefore, the hardness decreases.

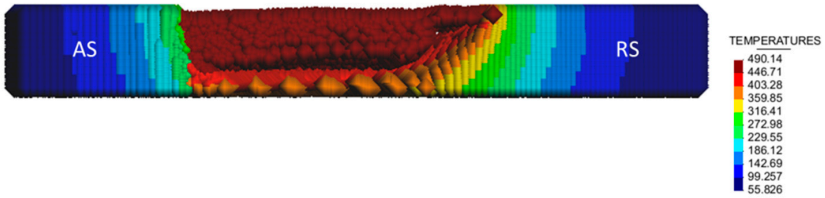

Figure 12. Maximum temperature tracked on the material tracers.

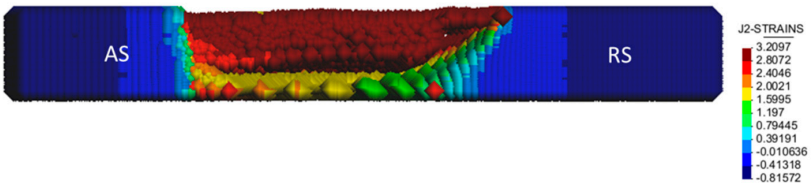

Figure 13. Maximum equivalent strain rate tracked on the material tracers (in logarithmic scale).

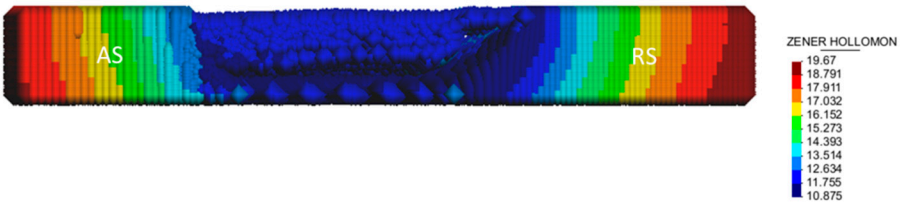

Figure 14. Zener-Hollomon parameter tracked in the material tracers (in logarithmic scale).

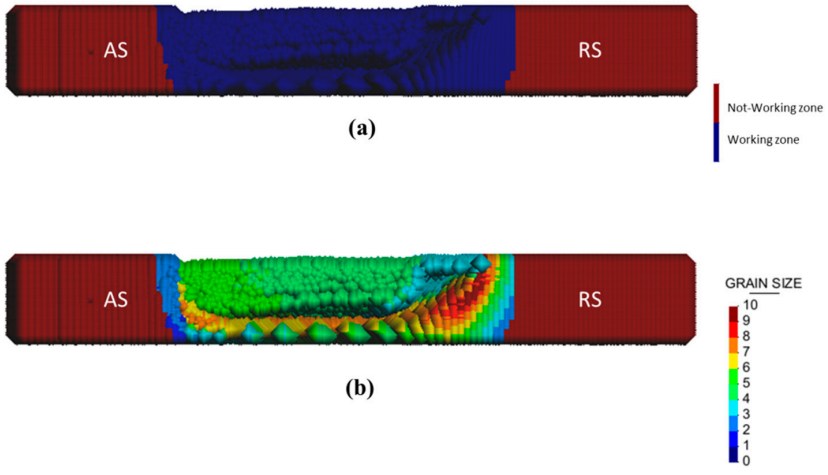

Figure 15. (**a**) Presentation of the working and non-working zones in the material tracers (**b**) Grain size in the material tracers.

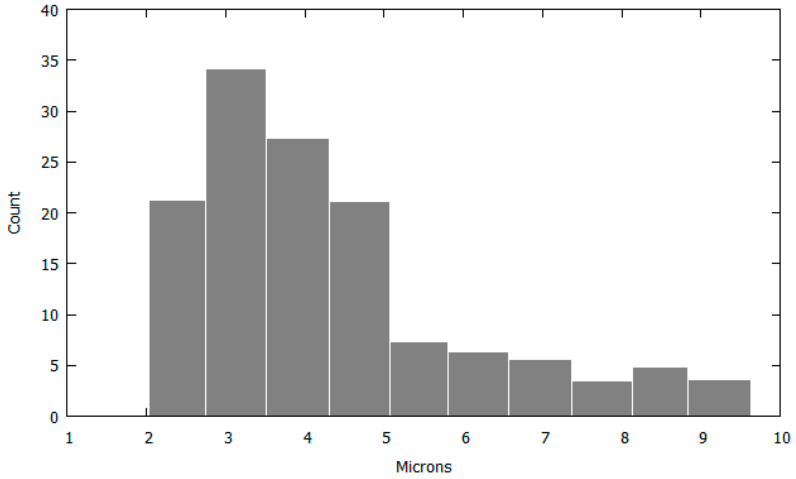

Figure 16. Histogram of grain intercept in friction stir processed sample (reproduced from [11]).

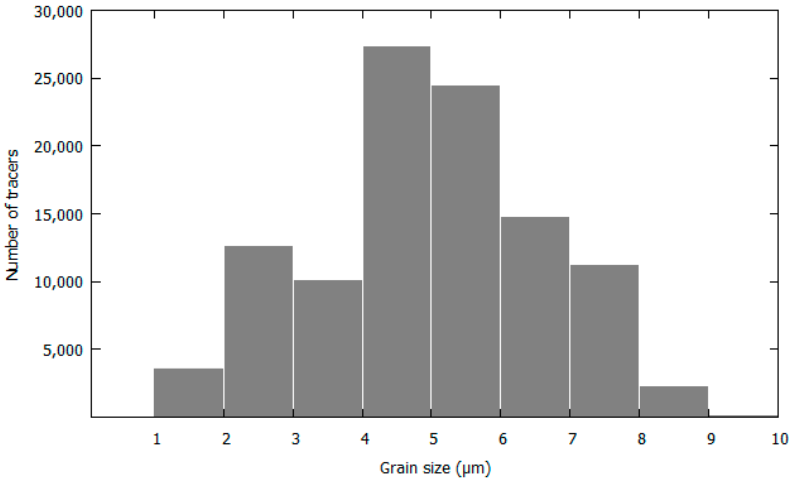

Figure 17. Grain size distribution on the tracers of the working zone.

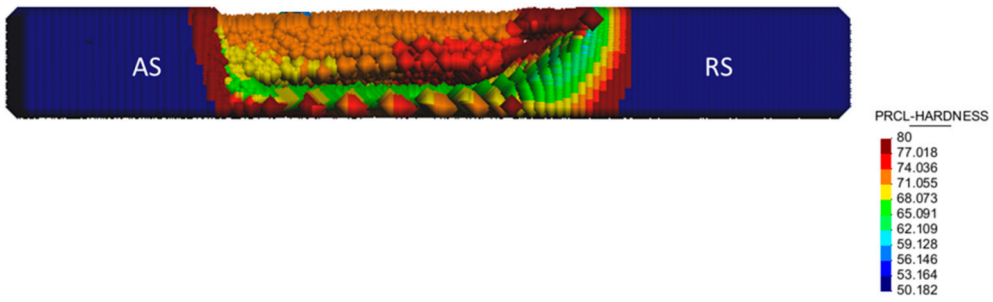

Figure 18. Vickers microhardness in the material tracers.

5. Conclusions

In this work, the computational prediction of metallurgical and microstructural aspects of the FSW processed material in terms of grain size and microhardness are discussed. Results are validated with experimental data from reference [11].

A two-stage procedure for decreasing the computational time is adopted. The local simulation of the FSW process is performed using an apropos kinematic framework to obtain equivalent strain rate and temperature values at finite element nodes. A material particle tracing technique is applied at

the second stage for tracking the material flow during the weld. The relationship among the resulting grain size, microhardness, and the applied working strain rate and temperature for the friction stir processing in the AZ31 Mg alloy is examined.

A log-linear description relates the average grain size to the Zener-Hollomon parameter. In turn, the Zener-Hollomon parameter relies upon the history of strain rate and temperature of the moving tracers located in the finite element model.

Compared to the experimental data, good agreement with the computational results is observed in terms of temperature, average grain size and microhardness. The results show evidence of grain refinement and homogenization of the microstructure. The resultant grain size is a consequence of the opposed effects of grain refinement, by increasing strain rate, and grain growth, by the temperature rise. As the temperature increases, the material softens due to grain growth and thus, the hardness decreases.

Acknowledgments: This research has received the financial support from the MINECO (Ministerio de Economia y Competitividad of the Spanish Government) through the ADaMANT project (ref. DPI2017-85998-P).

Author Contributions: N. Dialami, M. Cervera and M. Chiumenti developed the numerical model; N. Dialami analyzed the data.

Conflicts of Interest: The authors declare no conflict of interest.

References

1. Yuan, W.; Mishra, R.S.; Carlson, B.; Verma, R.; Mishra, R.K. Material flow and microstructural evolution during friction stir spot welding of AZ31 magnesium alloy. *Mater. Sci. Eng. A* **2012**, *543*, 200–209. [CrossRef]
2. Li, Y.; Qin, F.; Liu, C.; Wu, Z. A review: Effect of friction stir welding on microstructure and mechanical properties of magnesium alloys. *Metals* **2017**, *7*, 524.
3. Pashazadeh, H.; Teimournezhad, J.; Masoumi, A. Numerical investigation on the mechanical, thermal, metallurgical and material flow characteristics in friction stir welding of copper sheets with experimental verification. *Mater. Des.* **2014**, *55*, 619–632. [CrossRef]
4. Padmanaban, R.; Ratna Kishore, V.; Balusamy, V. Numerical Simulation of Temperature Distribution and Material Flow During Friction Stir Welding of Dissimilar Aluminum Alloys. *Procedia Eng.* **2014**, *97*, 854–863. [CrossRef]
5. Dialami, N.; Chiumenti, M.; Cervera, M.; de Saracibar, C.A.; Ponthot, J.-P. Material Flow Visualization in Friction Stir Welding via Particle Tracing. *Int. J. Met. Form.* **2013**, *8*, 167–181. [CrossRef]
6. Dialami, N.; Chiumenti, M.; Cervera, M.; de Saracibar, C.A.; Ponthot, J.-P. Numerical simulation and visualization of material flow in friction stir welding via particle tracing. In *Numerical Simulations of Coupled Problems in Engineering*; Springer International Publishing: Cham, Switzerland, 2014; pp. 157–169.
7. Masaki, K.; Sato, Y.S.; Maedab, M.; Kokawa, H. Experimental simulation of recrystallized microstructure in friction stir welded Al alloy using a plane-strain compression test. *Scr. Mater.* **2008**, *58*, 355–360. [CrossRef]
8. Zhang, Z.; Wu, Q.; Grujicic, M.; Wan, Z.Y. Monte Carlo simulation of grain growth and welding zones in friction stir welding of AA6082-T6. *J. Mater. Sci.* **2016**, *51*, 1882–1895. [CrossRef]
9. Chang, C.I.; Lee, C.J.; Huang, J.C. Relationship between grain size and Zener–Hollomon parameter during friction stir processing in AZ31 Mg alloys. *Scr. Mater.* **2004**, *51*, 509–514. [CrossRef]
10. Pan, W.; Li, D.; Tartakovsky, A.M.; Ahzi, S.; Khraisheh, M.; Khaleel, M. A new smoothed particle hydrodynamics non-Newtonian model for friction stir welding: Process modeling and simulation of microstructure evolution in a magnesium alloy. *Int. J. Plast.* **2013**, *48*, 189–204. [CrossRef]
11. Darras, B.M.; Khraisheh, M.K.; Abu-Farha, F.K.; Omar, M.A. Friction stir processing of commercial AZ31 magnesium alloy. *J. Mater. Process. Technol.* **2007**, *191*, 77–81. [CrossRef]
12. Ammouri, A.H.; Kridli, G.; Ayoub, G.; Hamade, R.F. Relating grain size to the Zener–Hollomon parameter for twin-roll-cast AZ31B alloy refined by friction stir processing. *J. Mater. Process. Technol.* **2015**, *222*, 301–306. [CrossRef]
13. Fratini, L.; Buffa, G.; Palmeri, D. Using a neural network for predicting the average grain size in friction stir welding processes. *Comput. Struct.* **2009**, *87*, 1166–1174. [CrossRef]
14. Saluja, R.S.; Ganesh Narayanan, R.; Das, S. Cellular automata finite element (CAFE) model to predict the forming of friction stir welded blanks. *Comput. Mater. Sci.* **2012**, *58*, 87–100. [CrossRef]

15. Dialami, N.; Chiumenti, M.; Cervera, M.; de Saracibar, C.A. An apropos kinematic framework for the numerical modeling of friction stir welding. *Comput. Struct.* **2013**, *117*, 48–57. [CrossRef]
16. Dialami, N.; Cervera, M.; Chiumenti, M.; de Saracibar, C.A. Local-global strategy for the prediction of residual stresses in FSW processes. *Int. J. Adv. Manuf. Technol.* **2016**, *88*, 3099–3111. [CrossRef]
17. Dialami, N.; Chiumenti, M.; Cervera, M.; de Saracibar, C.A. Challenges in thermo-mechanical analysis of Friction Stir Welding processes. *Arch. Comput. Methods Eng.* **2017**, *24*, 189–225. [CrossRef]
18. Dialami, N.; Chiumenti, M.; Cervera, M.; de Saracibar, C.A. A fast and accurate two-stage strategy to evaluate the effect of the pin tool profile on metal flow, torque and forces during friction stir welding. *Int. J. Mech. Sci.* **2017**, *122*, 215–227. [CrossRef]
19. Dialami, N.; Chiumenti, M.; Cervera, M.; Segatori, A.; Osikowicz, W. Enhanced friction model for Friction Stir Welding (FSW) analysis: Simulation and experimental validation. *Int. J. Mech. Sci.* **2017**, *133*, 555–567. [CrossRef]
20. Dialami, N.; Cervera, M.; Chiumenti, M.; Segatori, A.; Osikowicz, W. Experimental validation of a FSW model with an enhanced friction model: Application to a threaded cylindrical pin tool. *Metals* **2017**, *7*, 491. [CrossRef]
21. Wang, Y.; Lee, C.; Huang, C.; Lin, H.; Huang, J. Influence from extrusion parameters on high strain rate and low temperature superplasticity of AZ series Mg-based alloys. *Mater. Sci. Forum* **2003**, *426*, 2655–2660. [CrossRef]
22. Chowdhury, S.H.; Chen, D.L.; Bhole, S.D.; Cao, X.; Wanjara, P. Friction stir welded AZ31 magnesium alloy: Microstructure, texture, and tensile properties. *Metall. Mater. Trans. A* **2013**, *44*, 323–336. [CrossRef]
23. Feng, A.H.; Xiao, B.L.; Maz, Y.; Chen, R.S. Effect of friction stir processing procedures on microstructure and mechanical properties of Mg-Al-Zn casting. *Metall. Mater. Trans. A* **2009**, *40*, 2447–2456. [CrossRef]
24. Afrin, N.; Chen, D.L.; Cao, X.; Jahazi, M. Microstructure and tensile properties of friction stir welded AZ31B magnesium alloy. *Mater. Sci. Eng. A* **2008**, *472*, 179–186. [CrossRef]
25. Sheppard, T.; Wright, D. Determination of flow stress: Part 1 constitutive equation for aluminum alloys at elevated temperatures. *Met. Technol.* **1979**, *6*, 215–223. [CrossRef]
26. Tello, K.; Gerlich, A.; Mendez, P. Constants for hot deformation constitutive models for recent experimental data. *Sci. Technol. Weld. Join.* **2010**, *15*, 260–266. [CrossRef]
27. Huang, C.C.; Huang, J.C.; Lin, I.K.; Hwang, Y.M. Processing fine-Grained and Superplastic AZ31 Mg Tubes for Hydroforming. *Key Eng. Mater.* **2004**, *271–274*, 289–294. [CrossRef]
28. Fatemi-Varzaneh, S.; Zarei-Hanzaki, A.; Beladi, H. Dynamic recrystallization in AZ31 magnesium alloy. *Mater. Sci. Eng. A* **2007**, *456*, 52–57. [CrossRef]
29. Hu, H.; Zhang, D.; Pan, F.; Yang, M. Thermal-stress simulation of direct-chill casing of AZ31 magnesium alloy billets. *J. Wuhan Univ. Technol. Mater. Sci. Ed.* **2009**, *24*, 376–382. [CrossRef]
30. Rodriguez, A.K.; Kridli, G.; Ayoub, G.; Zbib, H. Effects of the strain rate and temperature on the microstructural evolution of twin-rolled cast wrought AZ31B alloys sheets. *J. Mater. Eng. Perform.* **2013**, *22*, 3115–3125. [CrossRef]
31. Salem, H.G.; Reynolds, A.P.; Lyons, J.S. Microstructure and retention of superplasticity of friction stir welded superplastic 2095 sheet. *Scr. Mater.* **2002**, *46*, 337–342. [CrossRef]